Genesis of Typhoon Chanchu (2006) from a Westerly Wind Burst Associated with the MJO. Part I: Evolution of a Vertically Tilted Precursor Vortex

WALLACE HOGSETT AND DA-LIN ZHANG

Department of Atmospheric and Oceanic Science, University of Maryland, College Park, College Park, Maryland

ABSTRACT

Although previous studies have shown the relationship between the Madden–Julian oscillation (MJO) and tropical cyclogenesis (TCG), many scale-interactive processes leading to TCG still remain mysterious. In this study, the larger-scale flow structures and evolution during the pregenesis, genesis, and intensification of Typhoon Chanchu (2006) near the equator are analyzed using NCEP's final analysis, satellite observations, and 11-day nested numerical simulations with the Advanced Research Weather Research and Forecast model (ARW-WRF). Results show that the model could reproduce the structures and evolution of a synoptic westerly wind burst (WWB) associated with the MJO during the genesis of Chanchu, including the eastward progression of a WWB from the Indian Ocean into the Pacific Ocean, the modulation of the associated quasi-symmetric vortices, the initial slow spinup of a northern (pre-Chanchu) disturbance at the northeastern periphery of the WWB, and its general track and intensification.

It is found that the MJO, likely together with a convectively coupled Kelvin wave, provides the necessary low-level convergence and rotation for the development of the pre-Chanchu disturbance, particularly through the eastward-propagating WWB. The incipient vortex evolves slowly westward, like a mixed Rossby–gravity wave, on the northern flank of the WWB, exhibits a vertically westward-tilted circulation structure, and eventually moves northward off of the equator. Results show that the interaction of the tilted vortex with moist easterly flows assists in the downtilt-right (i.e., to the right of the upward tilt) organization of deep convection, which in turn forces the tilted vortex to move toward the area of ongoing deep convection, thereby helping to partly decrease the vertical tilt with time. It is shown that despite several days of continuous convective overturning, sustained surface intensification does not commence until the vortex becomes upright in the vertical. A conceptual model is finally presented, relating the decreasing vortex tilt to convective development, storm movement, TCG, and surface intensification.

1. Introduction

In the western North Pacific (WNP) basin, few tropical cyclones (TCs) develop prior to June (i.e., the onset of the Asian monsoon), even though the necessary conditions for tropical cyclogenesis (TCG) persist year round (Gray 1998). Instead, trade easterlies dominate the WNP during the spring months, and the rare TCs that do develop during this premonsoon period are often associated with anomalous westerly equatorial winds that modulate the formation of TC precursor disturbances (Ritchie and Holland 1999). This is the case for Typhoon Chanchu, which developed in early May 2006.

The Madden–Julian oscillation (MJO; Madden and Julian 1994; Zhang 2005) is the dominant mode of intraseasonal variability globally, and its active phase was first discussed by Liebmann et al. (1994) as a favorable environment for TCG. Specifically, the MJO can be characterized as a wavelike disturbance that propagates eastward from the equatorial Indian Ocean into the WNP, and its active phase is associated with enhanced deep convection and westerly winds in the lower troposphere, the so-called westerly wind bursts (WWBs). Previous studies have established a connection between the active MJO and TCG not only in the WNP (Maloney and Hartmann 2001) but also in the eastern Pacific (Maloney and Hartmann 2000a; Molinari and Vollaro 2000), southern Indian (Bessafi and Wheeler 2006), and North Atlantic (Maloney and Hartmann 2000b; Mo 2000) basins. Barrett and Leslie (2009) showed that the MJO significantly modulates TC activity in all ocean basins

Corresponding author address: Dr. Da-Lin Zhang, Department of Atmospheric and Oceanic Science, University of Maryland, College Park, College Park, MD 20742–2425.
E-mail: dalin@atmos.umd.edu

worldwide through its modulation of low-level vorticity and deep convection. Furthermore, Frank and Roundy (2006) and Aiyyer and Molinari (2008) showed that the MJO enhances easterly shear near TCG locations, and Camargo et al. (2009) found that the enhanced humidity is the most important contribution of the active MJO to TCG.

Near-equatorial WWBs converge with easterly trades during the active MJO, not only enhancing deep convection but also facilitating the growth of cyclonic disturbances through barotropic energy conversions associated with zonal convergence and cyclonic shear that is maximized on the lateral flanks of the WWBs (Maloney and Hartmann 2001). These subsynoptic eddies can serve as precursors to TCG (Aiyyer and Molinari 2003), and if the eddies are continuously produced along the flanks of the WWBs, they can repeatedly spawn TCs (Molinari et al. 2007). In some situations, WWBs can modulate the development of twin TCs that are roughly symmetric about the equator (Lander 1990; Nieto Ferreira et al. 1996; Zhu et al. 2003).

Dickinson and Molinari (2002) showed that westward-propagating mixed Rossby–gravity (MRG) waves could develop during the convective phase of the MJO and serve as precursors to TCG. The MRG waves exhibit a westward vertical tilt because of the easterly vertical shear during the MJO (Frank and Roundy 2006). Dickinson and Molinari (2002) further found that deep convection prior to TCG develops not near the circulation centers of the MRG waves but rather to their north. As the westward-tilted MRG waves "transition" to tropical depression (TD)-type waves, deep convection develops closer to their centers and they move northwestward away from the equator. However, the northward translation and transition of the incipient equatorial disturbances to off-equatorial TCs still remain mysteries central to the issue of TCG during the active MJO. In addition, little has been discussed in the literature about the role of eastward-propagating Kelvin waves in TCG.

While the previous studies have established the relationship among the MJO, WWBs, and TCG, little is certain about the mechanisms by which they interact. Specifically, what is the importance of the associated WWB vortex, occurring at the synoptic scale, in initiating TCG? How is the low-level cyclonic circulation, which is necessary for triggering wind-induced surface heat exchange (WISHE) processes (Emanuel 1986), initially generated from the large-scale flows? In this series of studies, we attempt to address these issues by examining the multiscale processes involving the MJO (and likely a Kelvin and an MRG wave), WWBs, mesoscale convective systems (MCSs), mesoscale convective vortices

(MCVs), and convective-scale processes during the genesis of Typhoon Chanchu (2006).

The purposes of Part I of this series of studies are to (i) document the evolution of large-scale conditions associated with Typhoon Chanchu, from its incipient to typhoon stage, using the National Centers for Environmental Prediction (NCEP) final analysis (FNL) at 1.0° resolution and satellite observations; (ii) demonstrate that the general flow structures and organization of precipitation leading to the genesis of Chanchu could be reasonably duplicated by an 11-day cloud-resolving simulation using the Weather Research and Forecasting (WRF) model at the finest resolution of 2 km; and (iii) examine the evolution of the simulated westward-tilted vortex associated with a WWB, hereafter the tilted WWB vortex, that leads to the genesis of Chanchu.

The next section provides an overview of the evolution of Chanchu in relation to the large-scale environment as well as the 2006 typhoon season and intraseasonal variability. Section 3 describes the configuration of the WRF model used for the present study. Section 4 compares the simulation results to available observations prior to the genesis of Chanchu. Section 5 shows the mechanisms by which the pre-Chanchu disturbance develops and evolves during the genesis stage. A summary and concluding remarks are given in the final section.

2. Overview

a. TC activity in the Indian and western Pacific basins: Spring 2006

Chanchu was the second named TC of the 2006 Northern Hemisphere tropical season and the second to make landfall in Southeast Asia. The first TC, Cyclone Mala, began to develop in the Indian Ocean basin on 20 April (Fig. 1), intensified into a category-4 cyclone by 28 April, and after making landfall in Burma accelerated northeastward over mainland China and into the open Pacific. As Mala completed its extratropical transition, an area of active equatorial deep convection northeast of Papua New Guinea, denoted "PNG" in Fig. 1, spawned the prerequisite disturbance on 30 April that led to the second named storm of the 2006 season, Typhoon Chanchu. The pre-Chanchu disturbance appears to have originated in the Southern Hemisphere and crossed the equator as it moved erratically northwestward (Fig. 1). Nearly eight days after its formation, the pre-Chanchu disturbance began to organize on 7 May; it received the designation of tropical depression on 8 May, and by 10 May it became a typhoon. While the current study focuses on the formation of Chanchu, the next two subsections indicate that the near-equatorial formation of Mala two weeks
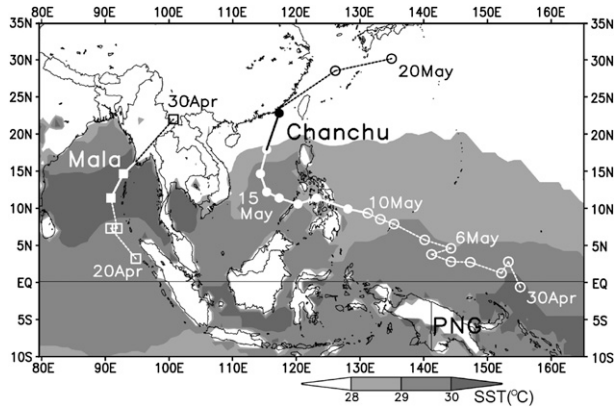
FIG. 1. Observed track of Typhoon Chanchu (Cyclone Mala), marked at daily (2-day) intervals and based on the 900-hPa circulation center from NCEP's FNL during the period of 0000 UTC 30 Apr–20 May 2006 (20–30 Apr). Filled symbols and heavy track lines represent the periods when the intensity exceeded a category-1 hurricane equivalent. NCEP SSTs at the model initial time are shaded according to the grayscale. "PNG" denotes the location of Papua New Guinea.

FIG. 2. Hovmöller diagram of the observed (5-day) mean MJO index from 27 Mar to 2 Jun 2006 for the equatorial region (30°S–30°N) spanning 80°–160°E, which is calculated as normalized deviations from the time-lagged patterns of the first extended EOF of 200-hPa velocity potential. Positive (negative) magnitudes are plotted using solid (dashed) contours at intervals of ± 0.2 and 0.5 and represent convectively inactive (active) periods. Convectively active periods are shaded according to the grayscale. The genesis periods of Chanchu and Mala are marked by the heavy arrows. (Data source: www.cpc.ncep.noaa.gov/products/precip/CWlink/daily_mjo_index/mjo_index.html.)

prior to Chanchu was not necessarily coincidental. Their associated tropical disturbances were closely associated with the active phase of the MJO.

b. Relationship between Chanchu and the MJO

For the purposes of this study, we use the term *genesis* (or *TCG*) for the stage during which a weak low-level (900-hPa) cyclonic circulation (i.e., with the maximum surface wind of much less than 17.5 m s^{-1} in NCEP FNL) exhibits little intensity change for a period of at least 24 h, and the terms *pregenesis* and *intensification* to indicate the stages prior to and after TCG, respectively. The genesis periods for Mala and Chanchu are shown schematically in Fig. 2 against the background of the NCEP–Climate Prediction Center (CPC) MJO index during April–May 2006. During this period, the MJO exhibited its well-known eastward propagation from the Indian Ocean into the Pacific Ocean. Both Mala and Chanchu, despite developing in separate basins, began genesis during the convectively active phase of apparently the same MJO event. The pre-Mala disturbance developed first as a closed low-level circulation on 20 April near 100°E, and the pre-Chanchu disturbance emerged near 155°E during the MJO's local peak conditions (Fig. 2). Both disturbances translated west-northwestward during genesis and reached tropical storm intensity during the transition period between the active and inactive MJO. The precursors associated with Mala and Chanchu appeared to persist as weak but coherent low-level cyclonic circulations for 5 and 8 days,
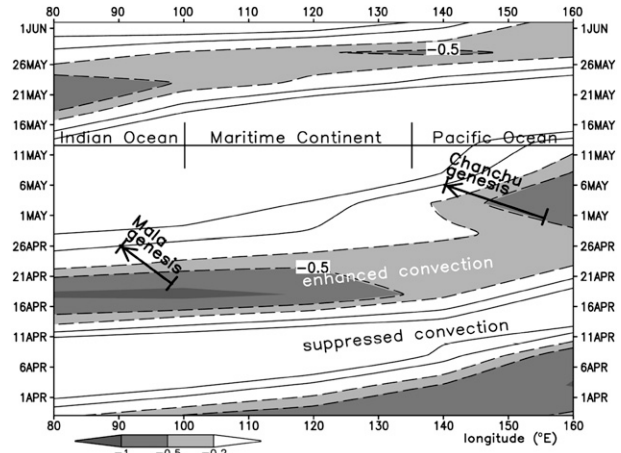
respectively, prior to being classified as tropical storms. It is likely that the slowly evolving MJO helped maintain the two TDs (Liebmann et al. 1994). While the pre-Mala and pre-Chanchu disturbances both developed during the active phase of the MJO, their genesis and subsequent intensification occurred as the MJO weakened (Fig. 2). Thus, the active phase of the MJO could not be considered as sufficient for TCG but only as favorable for TCG via its role in the development and maintenance of the pre-Mala and pre-Chanchu disturbances. Such precursor disturbances are a precondition for TCG.

It should be noted that the enhanced convection episode that spawned Mala and Chanchu was a relatively weak MJO event. Additionally, a conservatively estimated propagation speed from Fig. 2 is greater than 10 m s^{-1}, which is significantly greater than that for the typical MJO (4–8 m s^{-1}) (Sperber 2003; Zhang 2005). Instead, it falls within the range of a convectively coupled Kelvin wave (Straub and Kiladis 2003; Roundy 2008; Zhang 2005; Wheeler et al. 2000), whose signal is not excluded from the NCEP/CPC MJO index used to construct Fig. 2. Therefore, a convectively coupled Kelvin wave whose properties will be further shown later, superimposed on the weak MJO, might have some influences on the genesis of Chanchu. A detailed analysis of the equatorial wave activity, though outside the scope of the present study, could confirm this speculation.

c. Genesis of Chanchu

Enhanced deep convection and WWBs are well-known accompaniments to the MJO (and convectively coupled Kelvin waves) in the near-equatorial region. Figure 3 shows the synoptic setup at the 600- and 900-hPa levels during the pregenesis (prior to 30 April), genesis (30 April–7 May), and intensification (after 7 May) stages of Chanchu. A subtropical high pressure system dominated the WNP, with the easterly winds spanning the basin except in the vicinity of the equator. As early as 28 April, Fig. 3g shows a WWB situated on the Maritime Continent, extending eastward to PNG. Convergence of the WWB and the easterly trades led to enhanced cloud cover along their northwest–southeast-oriented interface (see Figs. 4a,b), with an inverted trough (see the dashed lines in Fig. 3g) just east of PNG in advance of the WWB. As discussed by Maloney and Hartmann (2001), the convergence of zonal winds and the presence of cyclonic shear can each contribute to the growth of eddies in the absence of significant planetary vorticity during the active MJO. The 900-hPa trough amplified as the WWB intensified to exceed 10 m s^{-1} and progressed eastward to nearly 160°E, and by late 30 April a closed cyclonic vortex developed to both the north ("C") and south ("L") of the WWB (Fig. 3h). By 2 May, two cyclonic vortices ("L") had developed south of the equator (Fig. 3i). Note that the two southern vortices resulted from the split of the WWB as it crossed the rugged terrain of New Guinea. Although the focus of the current study is the development of the northern vortex into Chanchu, it is noteworthy that New Guinea sits entirely in the Southern Hemisphere, and it likely disrupted the formation of a coherent mirror image vortex to that which formed in the Northern Hemisphere by 2 May.

A northwest–southeast-oriented trough also appeared at 600 hPa on 28 April (Fig. 3a) in advance of the WWB, but it was located about 1000 km to the west of the 900-hPa trough. By 2 May, two 600-hPa cyclonic circulations also appeared approximately symmetrically on the northern and southern sides of the WWB (Fig. 3c). Because the highest mountain on the island (i.e., Puncak Jaya) has an elevation of 4884 m, the WWB at 600 hPa showed little evidence of splitting. Note that the center of the northern 600-hPa circulation appeared as if it were spatially disjoint westward from its 900-hPa counterpart (cf. Figs. 3c,i) and that the WWB at 900 hPa extended much farther eastward than that at 600 hPa on 2 May. As will be shown in the next subsection, the two vortices are physically related in the vertical.

During the period of 2–6 May, the 600-hPa circulation moved slowly northeastward (Figs. 3c–e), while the 900-hPa vortex moved northwestward (Figs. 3i–k). The

northwestward movement of such low-level pre-TD disturbances during the active MJO period has been shown by Maloney and Hartmann (2001) and other studies. Because of their differing translations during 2–6 May, the horizontal distance between the two vortex centers diminished to nearly zero by 6 May, after which they moved northwestward as a vertically stacked vortex (Figs. 3f,l). The subsequent rapid convective organization and surface intensification after the two vortices were vertically locked in phase is evident on 10 May (see Fig. 4g). In fact, Chanchu nearly reached typhoon strength on this date.

The WWB that spawned the Chanchu precursor surged first rapidly eastward during 28 April–2 May, during which period it behaved as an eastward-propagating Kelvin wave (Zhang 2005). This surge resulted in the formation of the pre-Chanchu depression at 900 hPa, but the WWB then retreated northwestward together with the storm during 2–8 May (Figs. 3i–l). This behavior is similar to, but at a time scale shorter than, the MJO composites shown by Kim et al. (2008) and other studies. Thus, the evolution of the WWB shown in Fig. 3 could be considered typical, although the mechanisms responsible for the northward movement of the WWB are still not well established (Jiang et al. 2004). While we do not address this issue herein, it is of interest that because only the northern vortex intensified (and the southern one weakened due likely to the landmass blocking), its subsequent northwestward translation could give the appearance of the northwestward translation of the WWB.

As the eastward-moving WWB increased its intensity during 28 April–2 May, the pre-Chanchu disturbance amplified, likely because of the well-known mechanisms of barotropic eddy kinetic energy conversions (Maloney and Hartmann 2001) and wave accumulation (Sobel and Maloney 2000; Kuo et al. 2001). Once a closed vortex circulation developed (i.e., on late 30 April), it persisted for 7 days with little intensity change despite the continuous development of deep convection in its vicinity (Fig. 4). The pre-Chanchu depression did not undergo intensification, however, until it finally moved poleward of 5°N by 7 May, while the southern disturbance remained in close proximity to PNG and weakened with time (see Figs. 3f,l).

d. Mean structures of the MJO and WWB

Figure 5 shows the mean structures of the WWB and its associated dual (actually triple) vortices that occurred during the genesis phase of Chanchu. Note that the peak mean WWB occurred near 2°S. One could expect the development of twin vortices symmetrically located in each hemisphere if the WWB were symmetric about the equator. But with the mean WWB shown in Fig. 5,
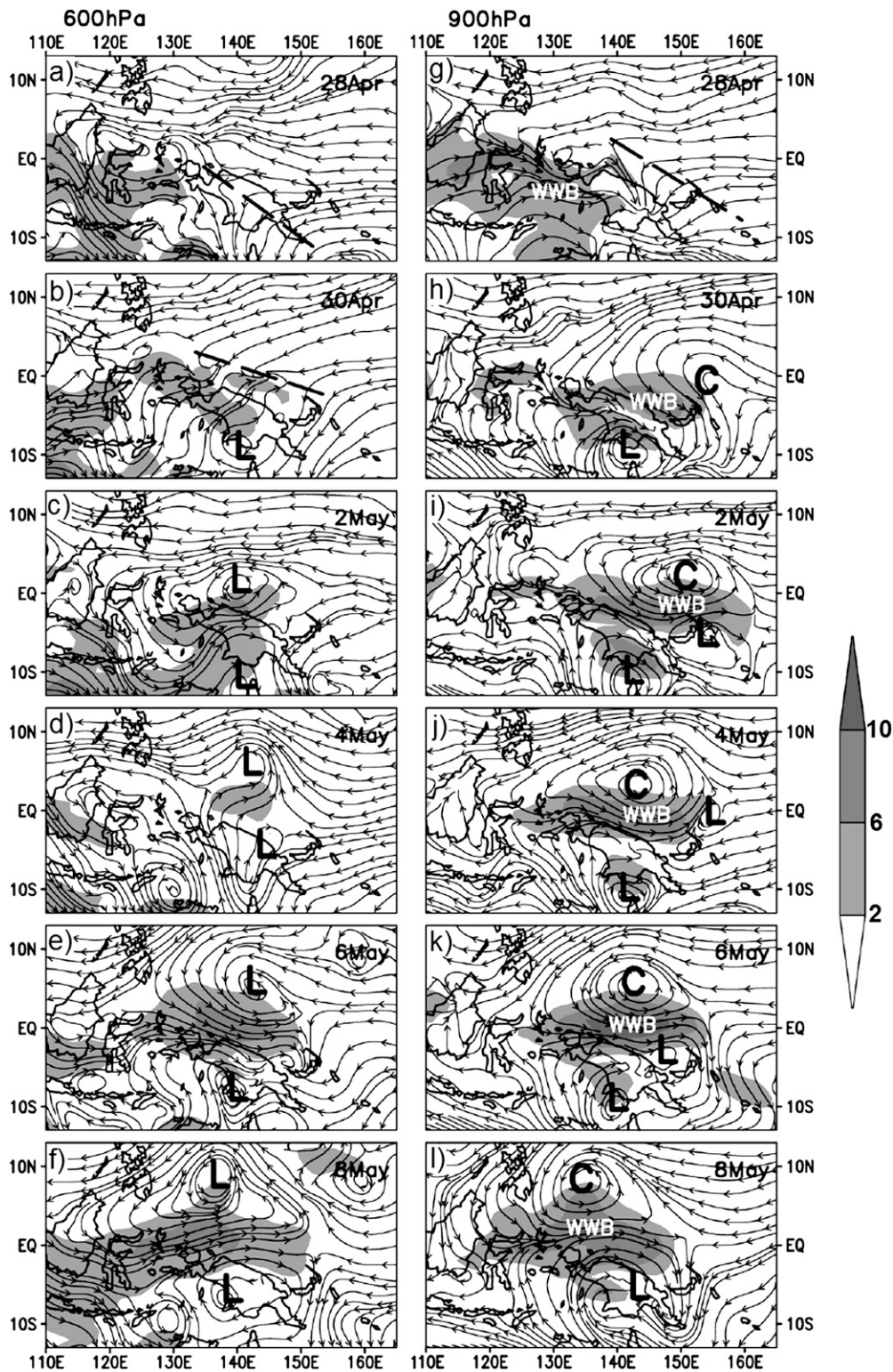
FIG. 3. Distribution of horizontal streamlines, obtained from NCEP's FNL, with the westerly winds (m s^{-1}) shaded in (a)–(f) at 600 hPa and (g)–(l) at 900 hPa during the period of (top) 0000 UTC 28 Apr to (bottom) 0000 UTC 8 May at 2-day intervals. Letter "C" highlights a closed 900-hPa circulation associated with Chanchu, and "L" denotes other closed cyclonic circulations. WWB denotes the westerly wind burst, and heavy lines represent trough axes of interest. Fields are averaged within a ±6-h period and a ±50-hPa layer.
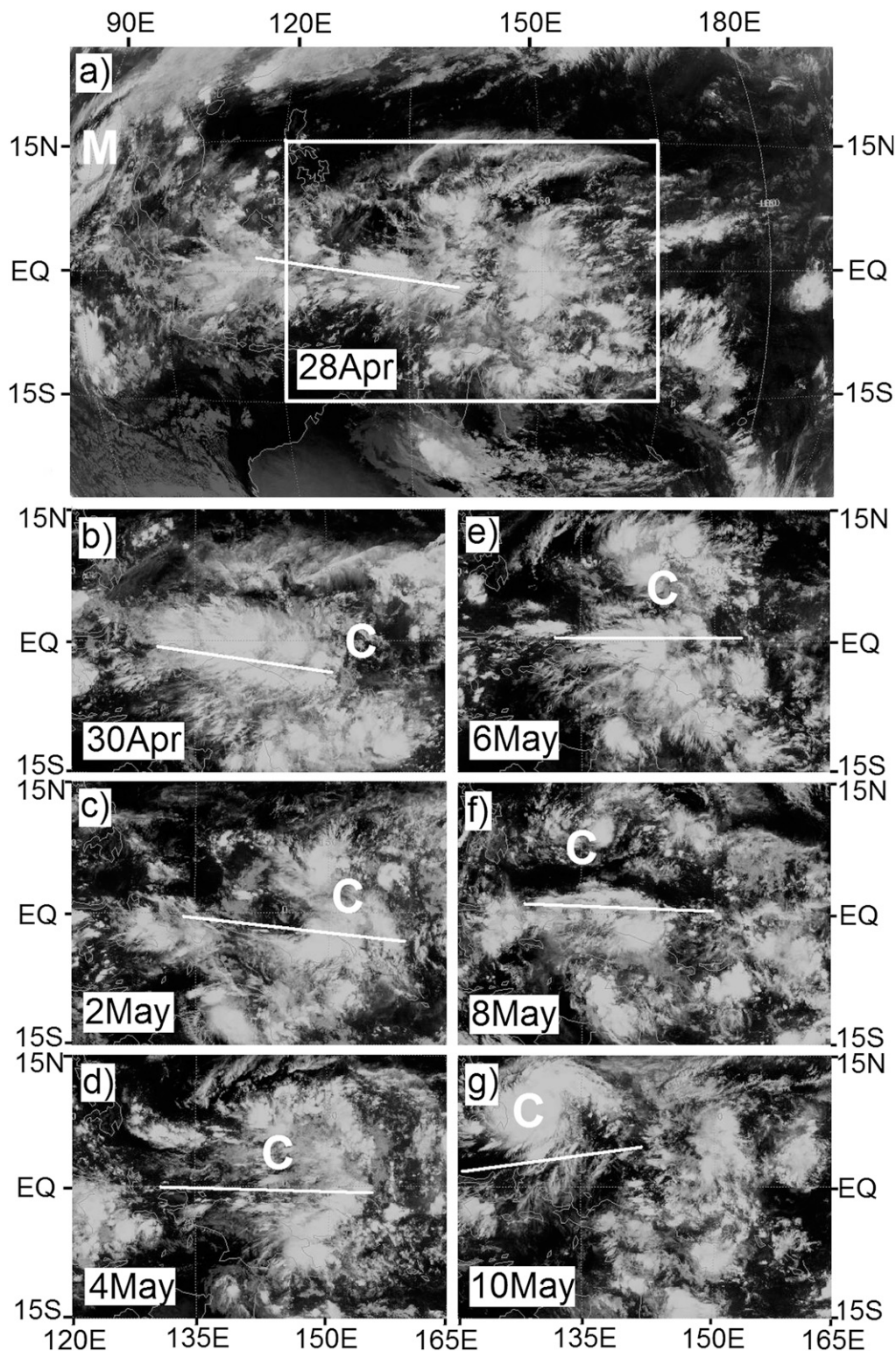
FIG. 4. Cloud fields as viewed from the *Multifunctional Transport Satellite* (*MTSAT*) infrared channel (10.3–11.3 μm) at 2-day intervals from (a) 0000 UTC 28 Apr to (g) 10 May 2006. The box in (a) denotes the region containing the pre-Chanchu disturbance (marked by a ''C'' during 30 Apr–10 May), and the solid line in (a)–(g) denotes the axis of the WWB at 900 hPa. In (a), Cyclone Mala (marked by ''M'') is shown just prior to its landfall on 28 Apr. (Data source: http://www.ncdc.noaa.gov/gibbs/.)
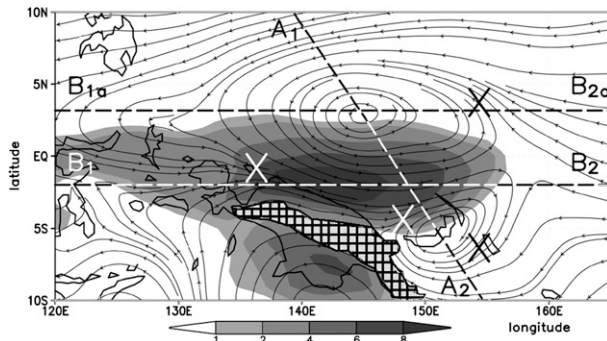
FIG. 5. The 900–800-hPa layer-mean horizontal streamlines, with the westerly flows shaded (m s^{-1}), that are averaged during the period of 30 Apr–5 May 2006 from NCEP's FNL. Lines A_1–A_2, B_1–B_2, and B_{1a}–B_{2b} represent the paths of the vertical cross sections, shown in Fig. 6, through the centers of the quasi-symmetric cyclonic vortices, along the axis of the WWB, and through the pre-Chanchu vortex, respectively. The "X" marks the areas of obvious low-level confluence, and areas of underlying terrain are hatched.

FIG. 6. Vertical cross sections of horizontal wind barbs (a full barb is 5 m s^{-1}) and the vertical relative vorticity (±1, 1.5, 2, 2.5, and 3×10^{-5} s^{-1}, contours), as shown in Fig. 5, with westerly flows shaded (m s^{-1}), that are taken (a) across the composite WWB (i.e., line A_1–A_2) and (b) along the axes of the WWB (line B_1–B_2) and through the pre-Chanchu vortex (line B_{1a}–B_{2b}). Solid (dashed) contours denote positive (negative) relative vorticity, and only the positive values in (b) are shown. Note that in (b) only the relative vorticity field is taken along (B_{1a}–B_{2b}) to show the WWB-associated vorticity field. Fields are calculated as a five-gridpoint slice average.

the southern vortex should be more dynamically favored for TCG because of the presence of a larger Coriolis force. However, as discussed earlier, the southern vortex developed in the vicinity of the large landmass of New Guinea, which tended to disrupt intensification. Evidence of the second southern vortex can be seen near 10°S in association with the southern (and weaker) split of the WWB. Further, the northward movement of the WWB at later stages favored the northern vortex. Thus, in extraordinarily fortuitous situations twin TCs could develop and exhibit a mirror image about the WWB (e.g., see Zhu et al. 2003), but the present case is not such a scenario because of the island of New Guinea and the northward movement of the WWB that inhibited the southern vortices. Regardless of the fate of the southern vortices, the northern WWB vortex could be viewed as a westward-propagating MRG wave (Dickinson and Molinari 2002; Zhang 2005) within the mean easterly flow. Clearly the MJO—through enhanced low-level confluence (see the "X" symbols in Fig. 5) associated with the WWB, barotropic eddy growth, and northward movement into the open ocean, as well as the likely influences of Kelvin and MRG waves—created a favorable environment for TCG in the Northern Hemisphere.

Figure 6 shows the across- and along-flow vertical structures of the mean WWB. Across the WWB (Fig. 6a), easterly winds dominated the WNP basin except for its depth, which was confined below 400 hPa with the peak magnitude near 900 hPa. Associated with the WWB were the two lower-tropospheric cyclonic vortices exhibiting peak magnitudes at the interface of the westerly and easterly flow. An along-WWB vertical cross section clearly shows a westward tilt of the WWB with height
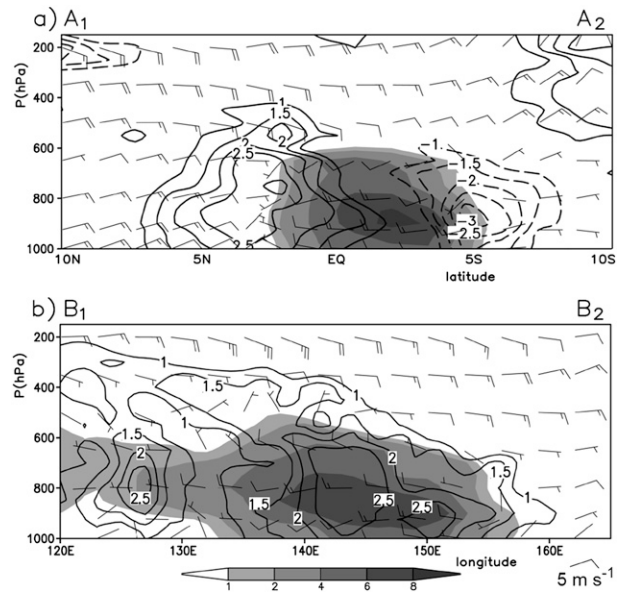
(Fig. 6b). At 800 hPa, the leading edge of the WWB extended to near 158°E, and its back edge was located much farther to the west of 120°E, giving it a horizontal scale of more than 4000 km. The westward vertical tilt explains the development of a closed 600-hPa circulation (Fig. 3c) over 1000 km to the west of the 900-hPa counterpart. The coherent vorticity structure north of the WWB (Fig. 6b) suggests that *the two circulations (i.e., at 900 and 600 hPa) could be considered as part of the same vertically tilted vortex*, which developed in the presence of large-scale easterly vertical shear (Fig. 6b).

In summary, the development of Chanchu could be traced back more than a week prior to its classification as a tropical depression and more than 10 days as a tropical disturbance. It formed at the leading portion of a synoptic-scale WWB associated with the eastward propagation of the MJO, which was influenced by an eastward-propagating Kelvin wave, and its associated vortex exhibited a westward tilt in the vertical. The subsequent northwestward movement of the Chanchu vortex could be attributed to the combined effects of a westward-propagating MRG, the β effect (Li and Wang 1994), and convective forcing. The ongoing processes during

this genesis period, particularly those unobservable from the large-scale analyses, are the subject of many unanswered questions about TCG. The subsequent sections describe a cloud-resolving simulation of the development of Chanchu (from its pregenesis to intensification) that is performed to replicate the above-observed evolution and attempt to gain insight into the processes by which the vertically tilted (synoptic scale) WWB vortex could transition into an intense typhoon.

3. Model description

The current study utilizes version 2.2 of the Advanced Research WRF model (ARW-WRF; Skamarock et al. 2005) to simulate for a period of 11 days the development of what would eventually become Supertyphoon Chanchu (2006) at the finest cloud-resolving resolution of 2 km. The model physics schemes used include (i) the Lin et al. (1983) cloud microphysics scheme (Tao et al. 1993), which contains six classes of water substance (i.e., water vapor, cloud water, rain, snow, graupel, and cloud ice); (ii) the Yonsei University planetary boundary layer (PBL) parameterization with the Monin–Obukhov surface layer scheme (Hong et al. 2006); (iii) the Rapid Radiative Transfer Model (RRTM) for long waves with six molecular species (Mlawer et al. 1997) and the Dudhia scheme for shortwave radiation; and (iv) a modified version of the Kain–Fritsch (Kain and Fritsch 1993) cumulus parameterization scheme for the outer three domains in which deep convection and a broad range of shallow convection are both parameterized. Note that no cumulus parameterization is used in the 2-km-resolution domain.

Figure 7 shows schematically the WRF model setup, which consists of a quadruply nested telescoping configuration. Three stationary outer domains A, B, and C have (x, y) dimensions of 100×134, 175×136, and 313×235 grid points with grid lengths of 54, 18, and 6 km, respectively; and a moving inner domain D with 301×301 grid points is used to follow the center of Chanchu at the grid length of 2 km. All domains have 40 vertical sigma levels, and the model top is defined at 30 hPa.

The integration proceeds via a staggered initiation of the nested domains, in which Chanchu is allowed to spin up within each domain before a new domain is initiated. The simulated Chanchu is not permitted to cross the boundary of any nest at any time, and care is taken to prevent the initialization of any nest when precipitation is occurring near the boundaries. The outermost domain (A) is initialized at 0000 UTC 27 April 2006. Domain B begins 4 days later (i.e., at 0000 UTC 1 May). Domain C is activated at 1200 UTC 2 May, and domain D 12 h later at 0000 UTC 3 May. The 11-day simulation is chosen to capture different development
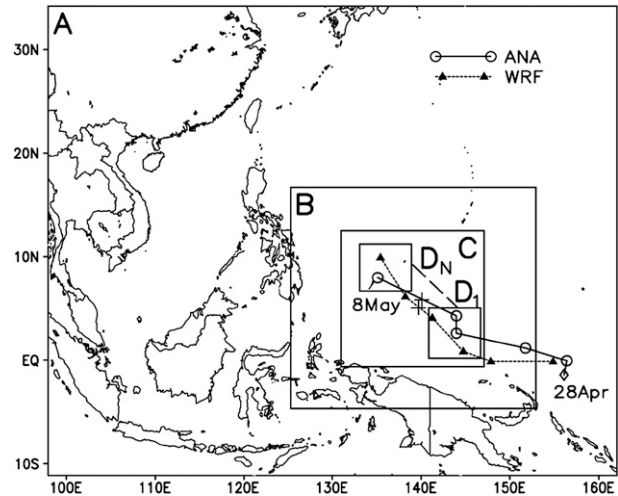

FIG. 7. Configuration of the nested WRF model domains. Domains A, B, and C remain fixed, while domain D moves with the storm along the dashed line between D_1 and D_N. The observed (solid with open circles) and simulated (dotted with filled triangles) tracks are shown at 2-day intervals from 28 Apr to 8 May 2006. The observed 28 Apr marker is diamond-shaped to denote the absence of a closed circulation, and it is placed at the location of peak vorticity near the 900-hPa trough. The plus signs along each track denote the approximate location where Chanchu began to intensify.

stages of Chanchu, including the earliest large-scale formation of a WWB associated with the MJO (domain A), the mesoscale genesis (domains B and C), and the storm-scale genesis and intensification (domain D). Because of the two-way interactive nature of the nests, we may use only the results from domain A to examine the large and mesoscale flows in Part I without losing the upscale influences of deep convection and the small-scale processes, which we reserve for subsequent studies.

The model initial conditions and the outermost lateral boundary conditions are obtained from NCEP FNL with the latter updated every 6 h. No artificial data (e.g., bogus vortices) are used during the 11-day model integration. Sea surface temperatures (SSTs) are updated daily using NCEP's data (see Fig. 1 for the initial SST distribution), though there is no significant TC-induced variation in SSTs during the simulation, as the disturbance remains weak. Note that the outermost domain A is allowed to spin up from the raw initial conditions in which the WWB has not yet moved across New Guinea and the pre-Chanchu disturbance has not yet developed into a closed circulation at any vertical level.

4. Model verification

In general, it is not surprising that the WRF model could reproduce well the large-scale features, given the NCEP FNL conditions at the lateral boundaries. Thus,

in this section we compare the 11-day WRF simulation to available observations of the track, intensity, and some major structures of the pre-Chanchu disturbance. It is evident from Fig. 7 that the model reproduces reasonably well the observed track, which was obtained by taking the location of the 900-hPa circulation center from NCEP FNL prior to Chanchu's depression stage and the Joint Typhoon Warning Center's (JTWC's) best-track analysis afterward. The simulation captures the formation of a low-level disturbance evident on 28 April near the equator at 155°E and its subsequent westward and northwestward translations up to 2 and 8 May, respectively.

While the observed disturbance remains quasi-stationary for about 2 days (i.e., 28–30 April), the simulated disturbance moves immediately westward, more like a pure MRG wave, likely because of the formation of a more intense disturbance than the observed, as will be discussed in the next paragraph. On 2 May, the simulated near-equatorial disturbance is displaced about 800 km to the west of the observed. After 2 May, both the simulated and observed disturbances begin to move northwestward away from the equator (cf. Figs. 7 and 3) until the end of the 11-day simulation on 8 May. At the final time, the simulated storm exhibits a track error of roughly 200 km northward compared to the observed. Despite these differences, especially for the premature westward translation, we may claim that the WRF model reproduces reasonably both the formation location near the equator and the subsequent movement of the storm for a period of 11 days. This indirectly confirms that the larger-scale flows, in which the weak disturbance evolves, are reasonably simulated.

The JTWC began to estimate the intensity of pre-Chanchu depression on 7 May, and their report suggests that the minimum pressure remained above 1000 hPa until 8 May (not shown) when the observed storm could be classified as a TS. Figure 8 shows that the simulated storm intensity remains nearly constant, with minimum pressure above 1000 hPa during the first 8-day (or 192-h) period, when few observations were available. However, it begins to intensify after the 192-h integration, valid at 0000 UTC 5 May (hereafter 5/00–192), which is more than 2 days earlier than the observed. This simulated early intensification could be attributed to its early west and northwestward translation during the period of 2–6 May (Fig. 7), when the simulated storm reaches its intensification position two days prior to that observed. Nevertheless, the intensifications of the observed and simulated storms occur at nearly the same position (i.e., near 5°N, 140°E; see Fig. 7). Thus, we may assume that the WRF model also reproduces reasonably the evolution of the storm intensity during the genesis stage.
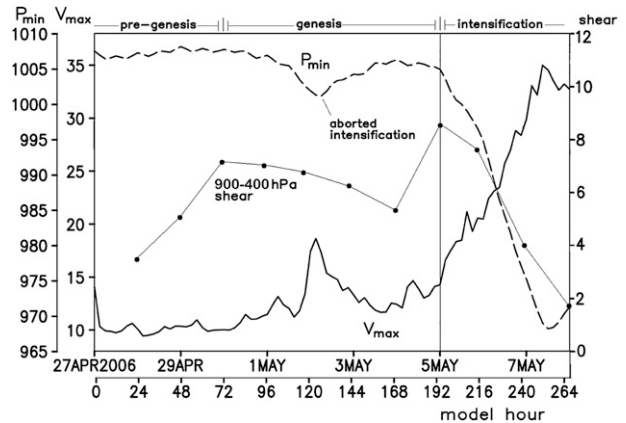

FIG. 8. Time series of P_{min} (hPa, dashed) and V_{max} (m s^{-1}, solid) at 3-h intervals, from the 11-day (i.e., 0000 UTC 27 Apr–0000 UTC 8 May 2006) simulation in domain A. The vertical wind shear (m s^{-1}) between 400 and 900 hPa is also superimposed at daily intervals, which is estimated using an area of 1000 km × 1000 km centered on the 900-hPa circulation center. The zonal component of the vertical shear is denoted at selected times. The thin solid vertical line at 0000 UTC 5 May demarcates the genesis and intensification periods.

Note that the simulated intensity changes (Fig. 8) can be clearly divided into three distinct stages: pregenesis, genesis, and intensification. During the genesis stage (i.e., after a closed low-level circulation develops but prior to sustained pressure falls, 30 April–5 May), the minimum central pressure P_{min} fluctuates between 1000 and 1007 hPa, and the maximum surface wind V_{max} fluctuates between 10 and 13 m s^{-1}. A noteworthy exception during the TCG stage is a near-equatorial *aborted intensification episode* (i.e., a temporary intensification and subsequent weakening before and after 2/00–120, respectively; Fig. 8). It is well known that TCG rarely occurs near the equator because of the lack of planetary vorticity for vortex stretching but, as will be shown in section 5, surface intensification can *temporarily* occur at this time because of increasing deep convection close to the low-level circulation center of the pre-Chanchu vortex. *Sustained* intensification begins at 5/00–192, which marks the end (beginning) of the genesis (intensification) stage. Subsequently, the storm deepens until 7/12–252 with a 36-hPa drop in P_{min} and an increase in V_{max} to about 35 m s^{-1}, just reaching typhoon intensity.

An examination of the large-scale VWS in the 900–400-hPa layer indicates that the synoptic environment in which the pre-Chanchu disturbance develops remains favorable for TCG (see Fig. 8), with VWS fluctuating between 2 and 9 m s^{-1} during TCG and intensification. The VWS during the early stages of TCG is primarily easterly because the 400-hPa flow over the equatorial region remains easterly (see Fig. 6), while the low-level

WWB surges eastward. This weak-to-moderate easterly VWS was generally favorable for TCG, especially during the aborted intensification.

Because direct observations of the storm intensity during TCG are not available, we compare in Fig. 9 the simulated sea level pressure and the vertically integrated cloud hydrometeors to the NCEP FNL and the satellite-observed outgoing longwave radiation (OLR) during the 11-day integration period. On 30 April, the model produces a loosely closed isobar of 1009 hPa at the equator—a surface manifestation of the pre-Chanchu disturbance, with dense cloud coverage near the circulation center (Fig. 9d). Although the simulated circulation translates faster than observed during 28–30 April and is thus located westward of that observed on 30 April (cf. Figs. 9a,d), as also indicated in Fig. 7, the model does capture the large area of cloud coverage observed to the north and west of the circulation as well as the cloud-free region to the southeast. Since the easterly trades increase with height (Fig. 6b), the upper-level hydrometeors tend to be advected downstream of the low-level convergence zone, forming a large area of stratiform clouds and precipitation to the northwest of the vortex (cf. Figs. 9d and 5).

Note that while the observed 900-hPa wind fields show *closed circulations* (denoted "C" and "L" in Figs. 9a–c), there are *no associated closed surface isobars* for either the pre-Chanchu or the Southern Hemispheric disturbance on 4 May (cf. Figs. 3i and 9b). Such a poor correspondence between the wind and mass fields is common over the equatorial area. Both the observed (Fig. 9b) and simulated (Fig. 9e) maximum cloud coverage shift from the western to the northern portion of the vortex during 30 April–4 May. Meanwhile, a cloud-free area develops to the south, suggesting large-scale dry intrusion and subsidence to the south of the vortex. The southern vortex evolves in close proximity to land with little intensity change, but the simulation captures well its associated cloud field on 4 May (Fig. 9e).

By 8 May both the observed and simulated storms exhibit easily identifiable centers in the sea level pressure fields as they deflect poleward and continue to intensify. The simulated Chanchu is much more intense than the observed on 8 May because of its premature intensification. However, despite the differences in intensity and some differences in the cloud coverage between the simulation and observations, their general agreement lends credibility to the 11-day simulation of the larger-scale environment. The ability of the WRF to reproduce the evolution of the WWB, which depends on the boundary conditions, is likely a significant reason for the success of the simulation.

5. The formation and evolution of the pre-Chanchu vortex

In this section we discuss in chronological order the formation of the closed pre-Chanchu circulation, the implications of its vertical tilt, the processes associated with the aborted intensification, and finally the transition of the tilted WWB vortex to an upright TC.

a. The formation of a closed pre-TC circulation

Understanding the origin of low-level disturbances is a challenging problem, and thus most TCG studies focus only on the amplification of pre-existing disturbances. In the present case, the eastward progression of the WWB appears to account directly for the formation of the pre-Chanchu disturbance. Although the MJO evolves with large-scale deep convection, the WWB and its associated vortices can be formed and maintained in the absence of deep convection, at least within this regional simulation in which the WWB is already present in the initial conditions. This is confirmed by a sensitivity simulation in which the effect of latent heating is turned off (hereafter the DRY run), while holding all the other conditions identical to the control run shown in section 4. It is found that the incipient WWB vortex in DRY forms at nearly the same location as that in the control run, but it fails to intensify (not shown), as expected.

To help visualize the formation of the pre-Chanchu disturbance, Fig. 10 shows a 3-day (i.e., 27/06–06 to 30/06–78) window of the simulated low- and midlevel flows in the vicinity of the WWB. In general, the model captures the eastward progression of the WWB (Figs. 10e–h), an inverted trough at both 600 (Fig. 10a) and 900 hPa (Fig. 10e), and the eventual development of closed circulations during this 3-day pregenesis period (Figs. 10d,h). Note that the inverted trough is already present in the model initial conditions because of the preexistence of the WWB (not shown), but it is quite weak. Note also that an easterly short wave (SW) approaches the WWB-related trough axis at 28/06–30 (Fig. 10f). According to Webster and Chang (1988), the trough axis at the leading edge of the WWB is a favorable region for wave accumulation. A possible example of this phenomenon is apparent between 28/06–30 and 29/06–54 (Figs. 10f,g) as the SW approaches the primary trough axis from the east.

Figures 10i–l show at higher time resolution the formation of the closed circulation at 900 hPa, which develops by 29/03–51 to the northeast of PNG where the SW merges into the preexisting trough axis. While deep convection may contribute to the trough amplification, it is not essential for the formation of the low-level closed circulation, since it also occurs in the DRY simulation
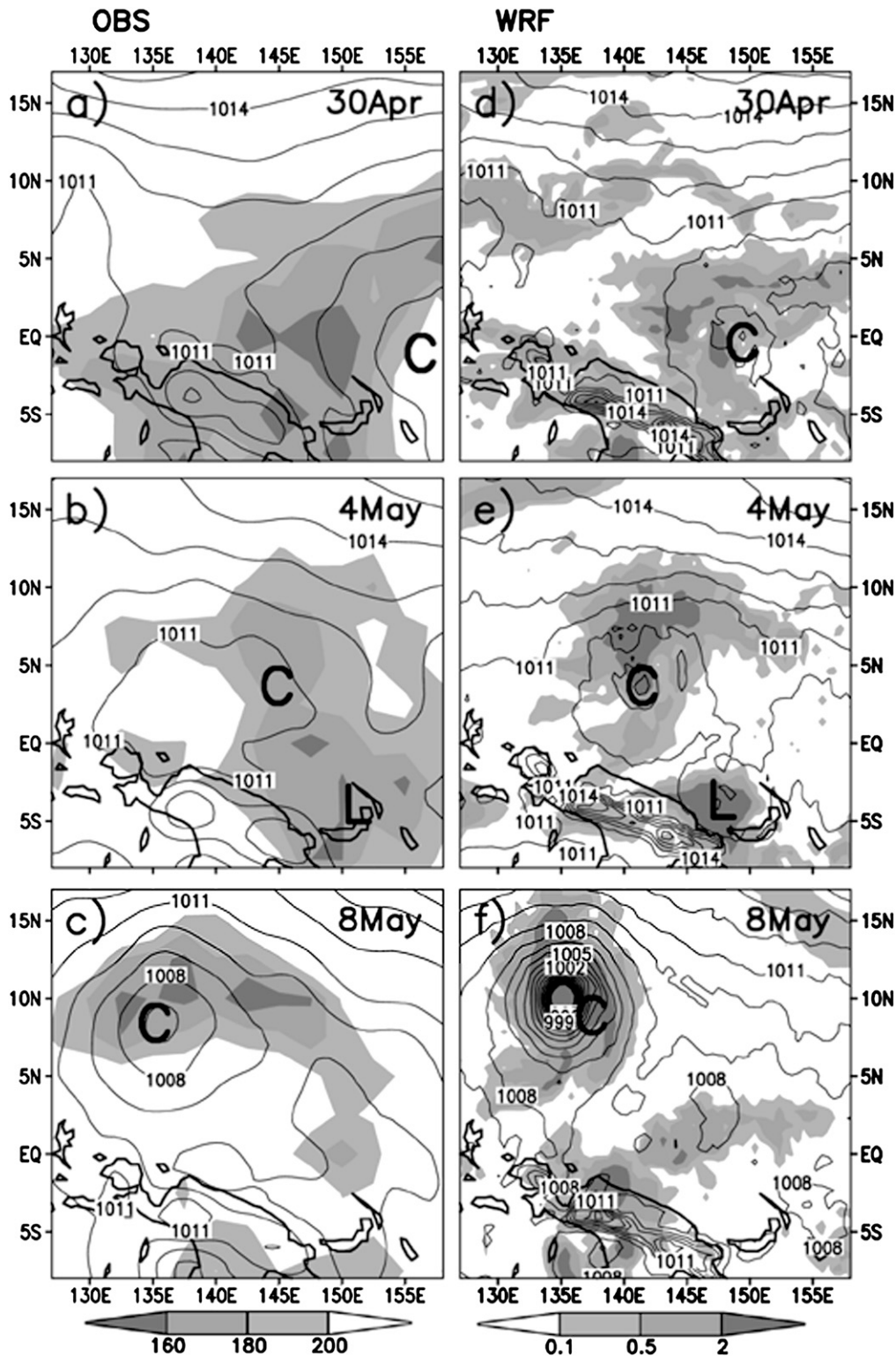
FIG. 9. Comparison of (a)–(c) the observed OLR (W m^{-2}, shaded) at the top of cloud columns with (d)–(f) the simulated vertically mass-weighted cloud hydrometeors (g kg^{-1}, shaded), and superimposed with contours of the sea level pressure (every 1 hPa) at 4-day intervals during the period of (top) 0000 UTC 30 Apr to (bottom) 8 May 2006. Fields in (d)–(f) are averaged during a 12-h period. (OLR data source: ftp://ftp.cdc.noaa.gov/Datasets/interp_OLR/olr.day.mean.nc.)
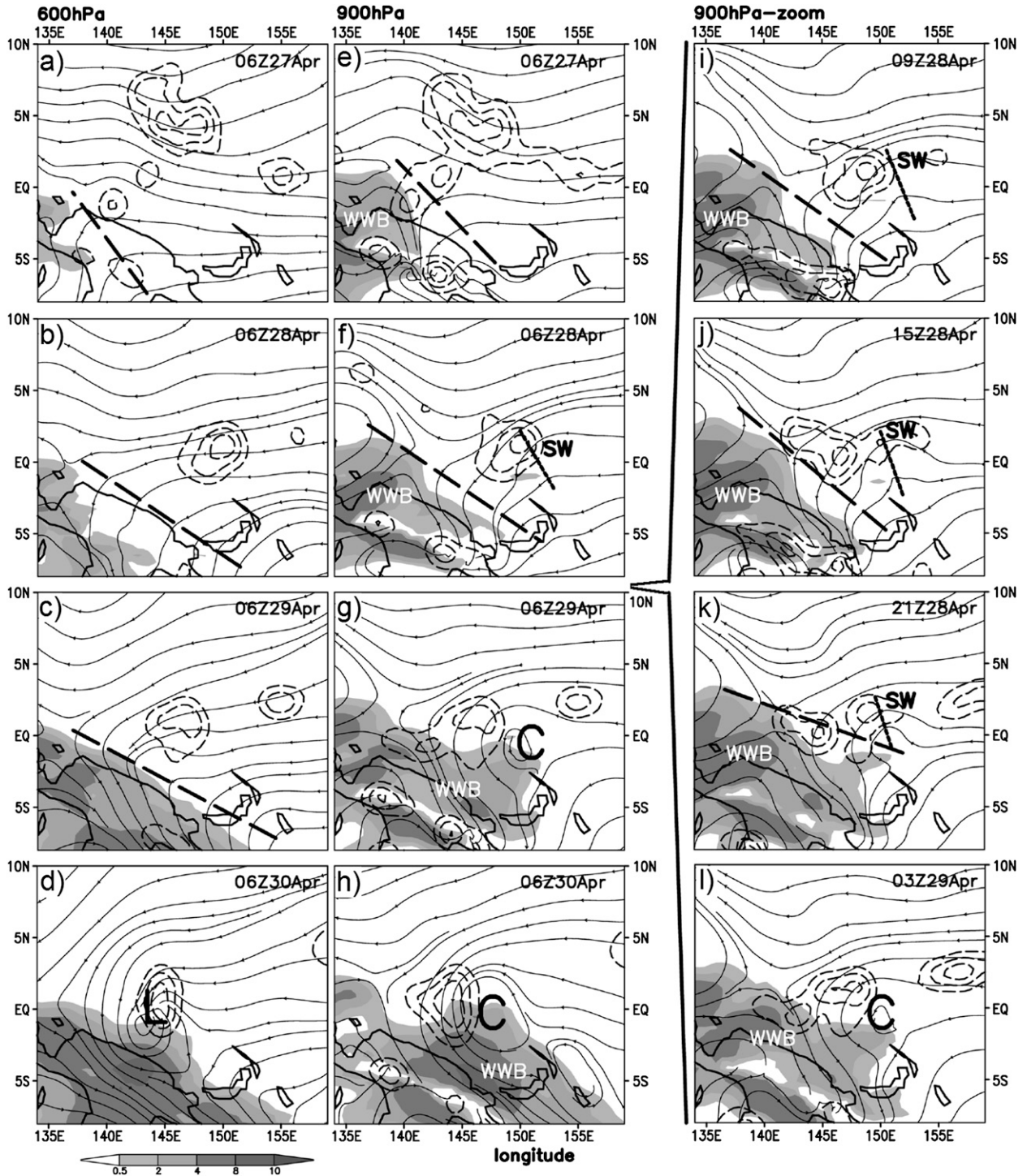
FIG. 10. (a)–(h) As in Fig. 3, but with radar reflectivity (5, 15, 25 dBZ, dashed contours) from (top) 0600 UTC 27 Apr to (bottom) 0600 UTC 30 Apr 2006 at daily intervals. (i)–(l) As in (e)–(h), but at 6-h intervals during (i) 0900 UTC 29 Apr to (l) 0300 UTC 30 Apr. Heavy dashed (dotted) diagonal lines denote major trough (SW) axes; "C" ("L") represents pre-Chanchu closed circulations at 900 hPa (600 hPa). Fields are averaged during a (left) 12-h or (right) 6-h period.

(not shown). As the WWB continues to penetrate eastward, the incipient 900-hPa disturbance progresses west-northwestward, with precipitation concentrated to the northwest of the 900-hPa center (Fig. 10h).

Although the SW does not show a clear signal in the 600-hPa streamlines (cf. Figs. 10b,f), its precipitation field approaches the pre-existing trough axis in a manner similar to that at 900 hPa but at a later time. That is, a closed cyclonic circulation does not occur at 600 hPa until 30/06–78 (Fig. 10d), which is 21 h later than that seen at 900 hPa because of the phase difference between the two levels. Both circulation centers develop roughly on the equator (Figs. 10d,h). In the DRY simulation, an inverted trough exists at 600 hPa at 30/06–78, but it does not exhibit a closed circulation (not shown). Thus, the distribution of a large area of mostly stratiform precipitation near the trough axis (Fig. 10d) suggests an important role of midlevel convergence in stretching the pre-existing vorticity for the formation of the pre-Chanchu vortex. This will be detailed in Part II (Hogsett and Zhang 2011, hereafter Part II).

b. Effects of the vertically tilted vortex

An important characteristic of the tilted WWB vortex is that organized deep convection occurs exclusively on the downtilt-right side of the vortex (i.e., to the right of the upward tilt; Fig. 10h). Little attention has previously been given to the relationship among the tilted vortex, convective organization, and TCG. Figure 11b shows that the tilted WWB vortex is characterized by a dipole of the vertically tilted potential temperature anomalies θ', with a positive θ' layer above a negative θ' layer. [Similar thermal anomalies also appear along the WWB axis to the south (not shown), indirectly confirming further the possible presence of a Kelvin wave (Straub and Kiladis 2003; Zhang 2005).] Such a vertical thermal structure is hydrostatically consistent with a tilted low pressure system that coincides *roughly* with the distribution of the vortex circulations. We believe that some mass-wind adjustment, despite occurring at a time scale much longer than that typically at higher latitudes (weekly to monthly), could still account for the generation of the tilted *synoptic-scale* vortex, given the thermal structures, or vice versa, over the equatorial region. Of course, this hypothesis should not be operative near the equator. In fact, the low-level subsynoptic flows, similar to those given in Fig. 11a, are nearly 90° cross-isobaric (not shown) beneath the elongated warm θ anomaly to the north-northwest of L_{900} (see Fig. 11a). This indicates that the balanced dynamics could not be applied to features at the subsynoptic or shorter scale in the present case.
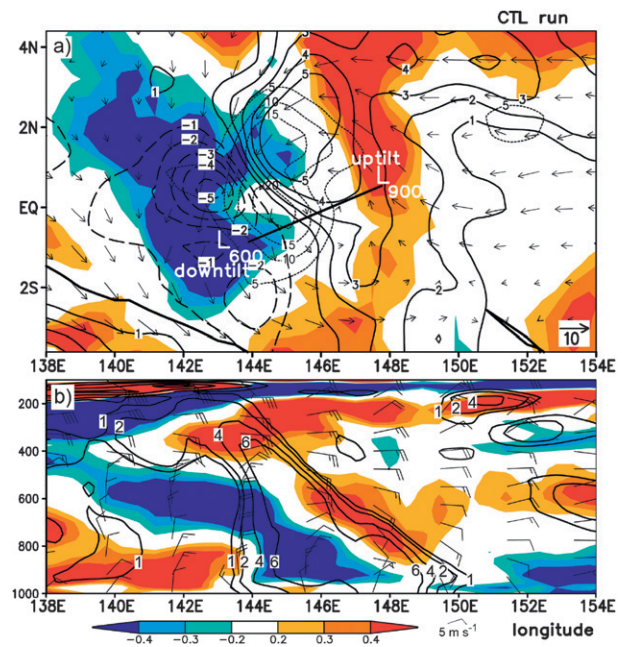

FIG. 11. (a) Horizontal distribution of the simulated mean θ' (K, shaded), radar reflectivity (dotted, every 5 dBZ), and vertical motion (solid: positive, dashed: negative; every 1 cm s^{-1}) at 700 hPa, valid at 0600 UTC 30 Apr ($\pm$3-h time mean). Horizontal wind vectors (700 hPa) and the vortex tilt (heavy solid line) between 600 hPa (L_{600}) and 900 hPa (L_{900}) are shown. (b) As in (a), but for the west–east vertical cross section along the equator of θ anomalies (shaded), relative vorticity (solid contours at 1, 2, 4, and 6 $\times$ 10^{-5} s^{-1}), and horizontal wind barbs.

Of interest is the phase relationship among the thermal anomaly, upward motion, and precipitation along any cyclonic streamline within the vortex (Fig. 11a). The distribution of precipitation to the west of the elongated warm anomaly suggests that the warming results likely from convectively generated compensating subsidence through the returning updrafts, often associated with presquall mesolows or troughs (see Hoxit et al. 1976; also see Fig. 3b in Zhang and Gao 1989). This subsidence argument is further confirmed by the dry run in which the warm anomaly is only limited to the vicinity of the vortex center.

A natural question one may ask is: why is deep convection favored in the northern but not the southern portion of the vortex? First, the possible existence of an eastward-propagating Kelvin wave indicates the presence of a surface-based (weak) cold pool along the WWB axis to the south of the vortex. Second, the MRG type of the WWB vortex favors low-level convergence to its east (Fig. 5). Third, while the large-scale VWS is weak to moderate (Fig. 8), the local VWS over the area between the low- and upper-level vortices where the wind direction is nearly opposite (e.g., see Figs. 13a–d) could

be more than 20 m s^{-1}, so deep convection in this overlapping area tends to be suppressed; this will be detailed in Part II. Fourth, an examination of the equivalent potential temperature θ_e field reveals the presence of higher-θ_e air in the incoming PBL easterly flow in the northern portion than in the westerly flow in the southern portion of the vortex (not shown).

Clearly, given the favorable conditions on the downtilt-right side of the tilted vortex, the resulting θ anomaly tends to cause isentropic ascent after air parcels pass the positive θ' ridge axis, enhancing the uplifting of the incoming high-θ_e air. The cyclonic downstream advection of cloud/precipitation particles and their subsequent evaporative cooling would induce moist downdrafts, enhancing the cold anomaly underneath the middle portion of the tilted vortex (cf. Figs. 11a,b). This, in addition to isentropic descent after passing the negative θ' ridge axis, diminishes the likelihood of convective development on the downtilt-left side of the vortex.

It should be mentioned that Fig. 11a suggests that the abovementioned dynamical/thermal and vertical motion relationship resembles that of the isentropic ascent (descent) on the downtilt-right (-left) side of an idealized TC-like vortex by Jones (1995). However, the two differ substantially in horizontal scale, degree of vertical tilt, and, more importantly, dynamic mechanisms (i.e., dry versus moist, barotropic versus baroclinic, balanced versus equatorial). The rainfall generation mechanism is also distinct from that in mature TCs, which exhibit enhanced upward motion on the downshear side (Zhang and Kieu 2006) and more clouds/precipitation on the downshear left side (Frank and Ritchie 1999; Black et al. 2002).

Because of the convectively generated lower surface pressures to the north and the presence of easterly flows, the low-level vortex center tends to move northwestward. Meanwhile, deep convection tends to increase the *midlevel* vorticity more than lower-level cyclonic vorticity to the north, as will be examined in Part II of this series of the papers, thus forcing the midlevel WWB vortex to move northeastward through horizontal convergence. This leads to the formation of an increasingly vertically erect vortex that could commence intensification as an upright TC. In their study of westward-tilting equatorial MRG waves during the MJO, Dickinson and Molinari (2002) found that precipitation occurred to the north of the waves, causing their transition into TD-type disturbances, but no mechanism for this transition was discussed. The results herein suggest that the tilted WWB vortex interacting with the moist easterly flows in the PBL provides a favorable environment for the organization of deep convection to the north, and then the convective forcing helps vertically align the cyclonic circulations, causing the subsequent intensification of

Chanchu. However, the vortex resiliency in the context of dry dynamics (Reasor et al. 2004) also plays an important role in vertically aligning the WWB vortex, since it occurs in the DRY run, too.

c. The aborted intensification

Although it is not possible to validate the aborted intensification, it is of interest to examine why TC intensification could temporarily occur near the equator and why it is later aborted. Prior to the aborted intensification at 1/15–111, there is an elongated area of precipitation on the downtilt-right side of the tilted vortex (see Figs. 11a and 12e). Thus, the intensification scenarios similar to those discussed in the preceding subsection occur during the 1/15–111 to 2/18–138 period, including the increased midlevel cyclonic vorticity by deep convection north of the surface low and the absorption of convectively generated vorticity by the WWB vortex. As a result, the vortex becomes nearly upright by 1/15–111 in association with an inner-core convective band that develops in a convergence zone about 30 km to the north of the low-level vortex center (see Fig. 12f). Because the latent heating occurs in the inner-core region, it is much more effective in spinning up the vortex than that in the outer region (Hack and Schubert 1986). It is important to note that even though the mid- and low-level circulation centers become nearly upright in the vicinity of the convective band, the outer regions of the vortex continue to exhibit vertical tilt, as indicated by the highly asymmetric circulation at 600 hPa. Thus, the tilted WWB vortex continues to support precipitation generation on the downtilt-right side during the aborted intensification period (Fig. 12). Again little precipitation occurs on the downtilt-left of the vortex.

As convection intensifies in the inner-core region, the maximum tangential winds increase rapidly (about 30%–40%) in a deep layer between 1/15–111 and 2/00–120 (Figs. 12e,f), while $P_{\min}$ falls from 1005 hPa to nearly 1000 hPa (Fig. 8). With the nearly upright vortex structure and organized deep convective bands in the inner-core regions, one may expect the beginning of sustained intensification at 2/00–120 (Figs. 12b,f). However, the convective bands weaken shortly after 2/00–120, likely because of the spread of cold downdraft air in the trailing stratiform region into the core region (Figs. 12e–g). Although the moist downdrafts at 900 hPa in the trailing stratiform region are generally less than 10 cm s^{-1} during the aborted intensification (Fig. 12f), they cover a large area of the western half of the vortex. Of course, TC intensification is not generally favored at such low latitudes ($\sim$1°N).

Once the inner-core deep convection weakens (Fig. 12g), convectively generated cyclonic vorticity tends to be

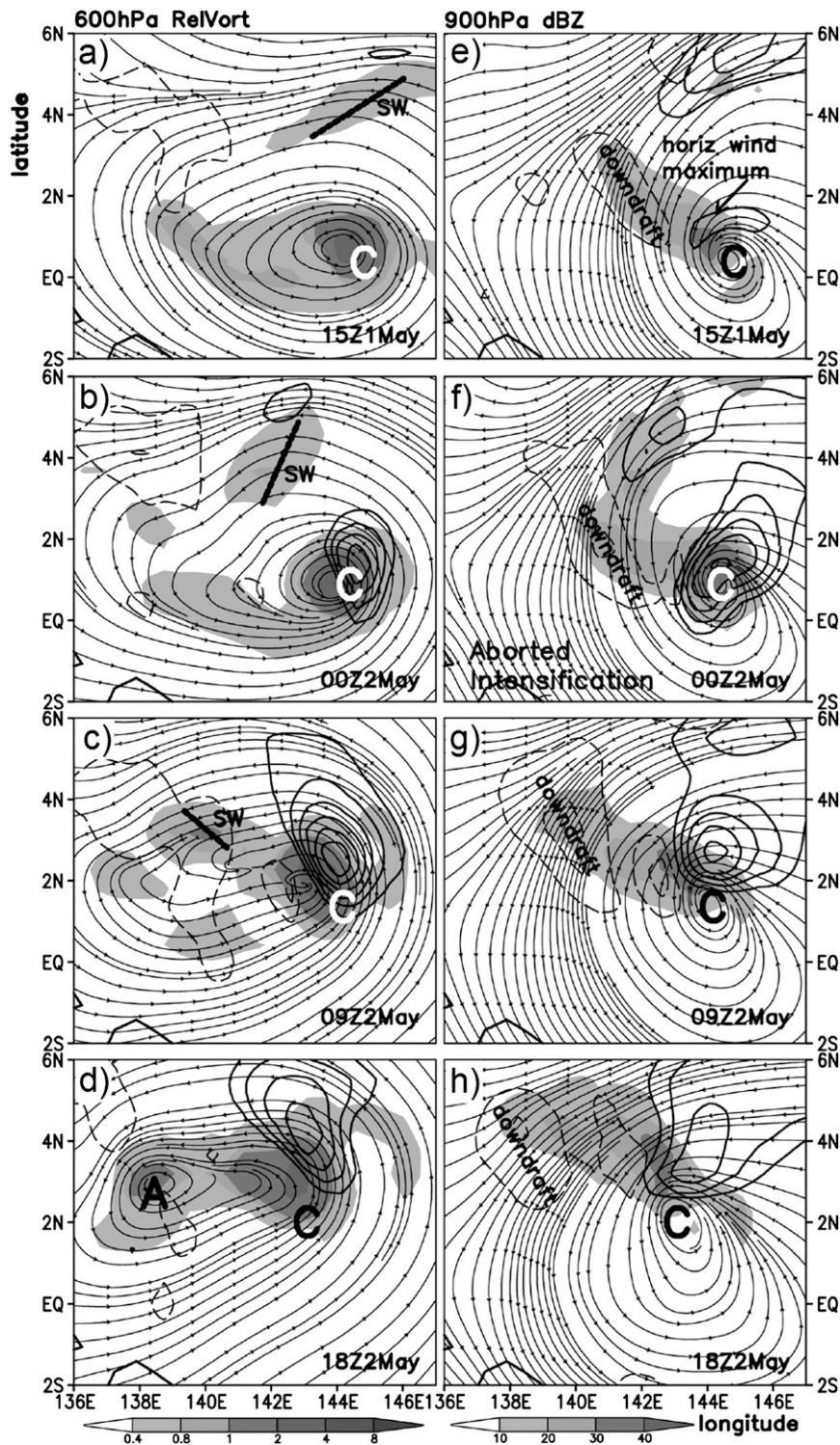FIG. 12. Horizontal distribution of (a)–(d) 600-hPa relative vorticity (shaded, $\times 10^{-5}$ s^{-1}) and (e)–(h) 900-hPa radar reflectivity (shaded, dBZ) at 9-h intervals, from (top) 1/15–111 to (bottom) 2/18–138 and superimposed with streamlines during the aborted intensification. Horizontal wind magnitude (thick solid contours at 14, 15, 16, 17, and 18 m s^{-1}), and descending motion (light dashed contours at 1, 5, 10, 20, 40 cm s^{-1}) are shown; "C" denotes the center of the 900-hPa closed circulation, and the heavy solid line in (a)–(c) denotes the location of an SW, which develops into the 600-hPa closed circulation "A". Fields are averaged within a ± 3-h period and a ± 50-hPa layer.

advected within the larger-sized tilted pre-Chanchu vortex, especially at the mid- and upper levels (Figs. 12c,d), and thus an increased vertical tilt appears again. Meanwhile, outside of the core region, another short wave becomes trapped within the midlevel circulation during the aborted intensification, likely assisting in the formation of a new closed vortex circulation "A" at 2/18–138 within the pre-Chanchu vortex (Fig. 12d). As a result, a broad west–east-oriented elliptically shaped midlevel vortex is tilted northwestward from the low-level circulation center (Figs. 12d,h).

d. Relationship between vertical tilt and intensification

Figure 13 shows the subsequent evolution of the pre-Chanchu disturbance after the aborted intensification, ultimately leading to sustained intensification. At 2/21–141—that is, 21 h after the aborted intensification (cf. Figs. 12b,f and 13a)—the vortex still exhibits a significant westward vertical tilt with a distance of about 500 km between the 900- and 600-hPa circulation centers, and deep convection with a large area of trailing stratiform precipitation confined on its downtilt-right side. However, the major rainband, which will be described in detail in Part II, is shifted far away from the 900-hPa circulation center (Fig. 12h) and is not as intense as that occurring during the aborted intensification. In the upper troposphere, easterly and southeasterly flows are diffluent (Fig. 13e) and generally favorable for TC intensification when combined with the vertical shear of below 10 m s^{-1} (Fig. 8).

By 3/15–159 (Fig. 13b), the orientation of the tilted vortex becomes more northwest–southeast (cf. Figs. 13a,b or 13h) as a result of differing movements between the low and midlevel circulations. That is, as discussed before, the surface low tends to move northwestward, while the convectively generated midlevel disturbances tend to force the midlevel circulations to move northeastward. Thus, the distance between the lower and midlevel circulation centers (i.e., the vertical vortex tilt) decreases with time. At 250 hPa, convective blocking leads to the northward deflection of the incoming easterly flow and pronounced diffluence behind the convective bands (Fig. 14f).

Subsequently, as the vertical tilt diminishes at 4/09–177, precipitation begins to wrap into the midlevel vortex (Fig. 13c), accelerating its spinup. By 5/03–195, the vortex becomes vertically coherent (Fig. 13d), nearly at the same time as the steady decrease in P_{min} commences (Fig. 8), signifying the beginning of TC intensification. A closed vortex circulation even could be seen at 250 hPa at this time (Fig. 13h). Note that even though the circulation *centers* are vertically coherent from 900 to 250 hPa, significant 900–600-hPa vertical shear (Fig. 13d) still exists in the far-field flow. The earlier rainband appears now as a spiral band, and the southern semicircle remains nearly precipitation-free as the previously distinct regions begin to intertwine. To summarize, the final two days of genesis can be characterized by an increasingly vertically upright, northwestward-moving vortex (i.e., from 900 to 250 hPa) as determined by the development of deep convection in the northern semicircle of the pre-Chanchu disturbance and the β effects, leading to the surface intensification by 5/00–192 (Fig. 13h).

6. Summary and conclusions

In this study, the larger-scale structures and evolution during the pregenesis, genesis, and intensification of Typhoon Chanchu are analyzed in the context of the early 2006 tropical season using NCEP's FNL, satellite observations, and 11-day numerical simulations with the ARW-WRF at the finest resolution of 2 km. It is found that the MJO, likely together with an eastward-propagating Kelvin wave, provided the necessary low-level convergence and rotation for the development of a precursor disturbance, particularly through a WWB that propagated near the equator from the Indian Ocean into the Pacific Ocean during late April 2006. It is shown that the 11-day simulation captures well many larger-scale features during the formation of Chanchu, including the propagation and structures of the WWB, the initial spinup of the pre-Chanchu disturbance at the eastern periphery of the WWB, and the general track and intensification of Chanchu. Although the simulated intensification begins two days prior to that observed, it occurs at nearly the same location along the track.

Figure 14 shows a conceptual model of several larger-scale processes leading to the development of Chanchu (2006), based on both the observations and model simulation. First, an eastward-moving deep WWB associated with the MJO facilitates the development of a westward-tilted cyclonic disturbance where the WWB interfaces with the easterly trades (Fig. 14a). Barotropic mechanisms likely play an important role in the formation of the closed circulation associated with the vertically tilted pre-Chanchu disturbance. Second, the tilted WWB vortex interacting with the moist easterly flows in the PBL assists in the organization of deep convection on its downtilt-right side, as also favored by the presence of relatively weak VWS and the low-level convergence associated with an MRG wave. Moreover, the vortex circulations at individual levels deviate northward toward the area of ongoing deep convection. Both the convective forcing and the dry dynamical vortex resiliency help decrease the vertical tilt of the WWB vortex.
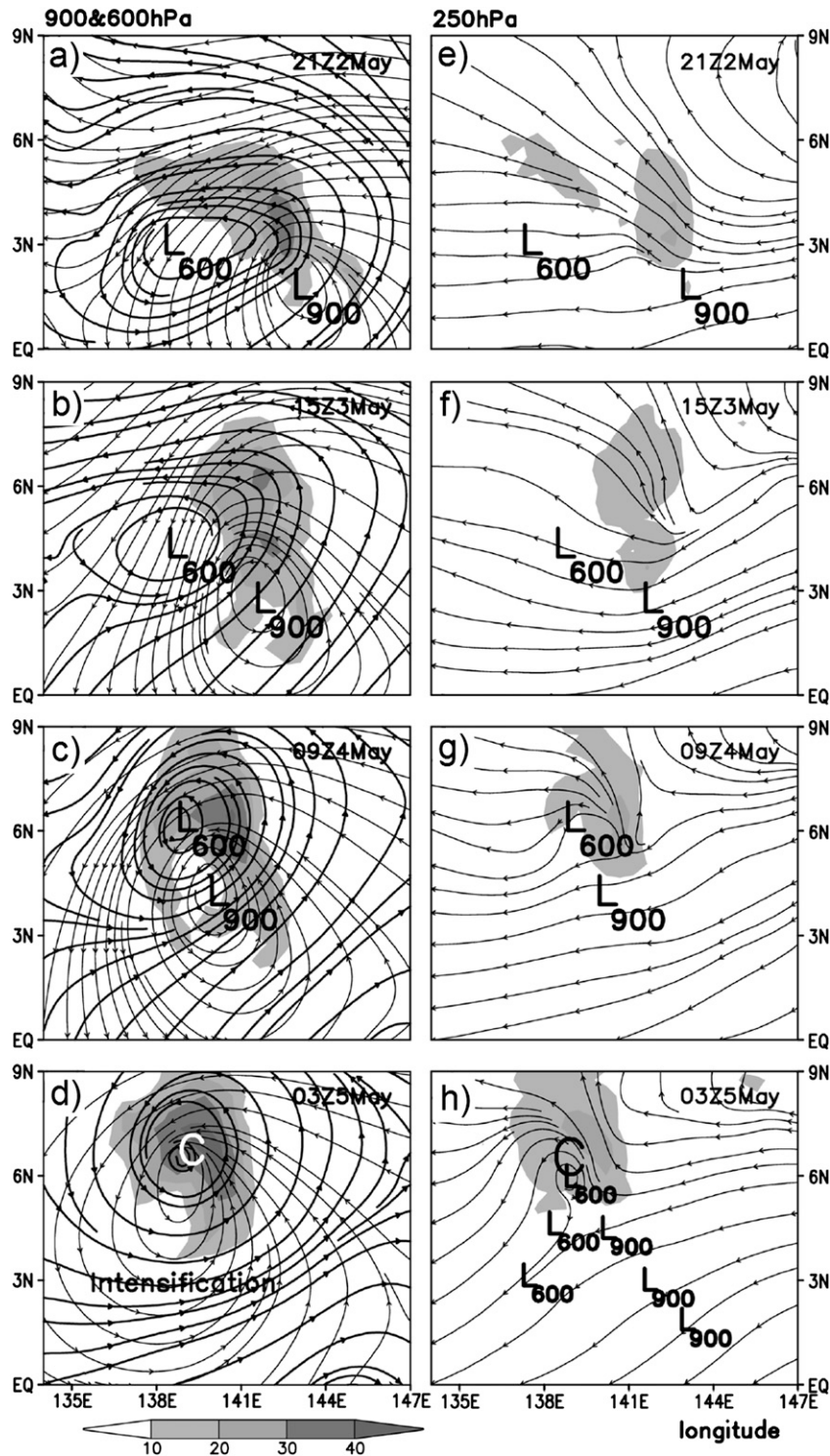
FIG. 13. Horizontal distribution of the radar reflectivity (shading, dBZ) and streamlines at (a)–(d) 900 hPa and (e)–(h) 250 hPa from (top) 2/21–141 to (bottom) 5/03–195 at 18-h intervals. In (a)–(d) 600-hPa streamlines are superposed to show the diminishing vertical tilt of the pre-Chanchu vortex. The 600- and 900-hPa circulation centers are denoted L$_{600}$ and L$_{900}$, respectively, until the intensification of Chanchu (''C'') has commenced. Fields are averaged within a $\pm$3-h period.
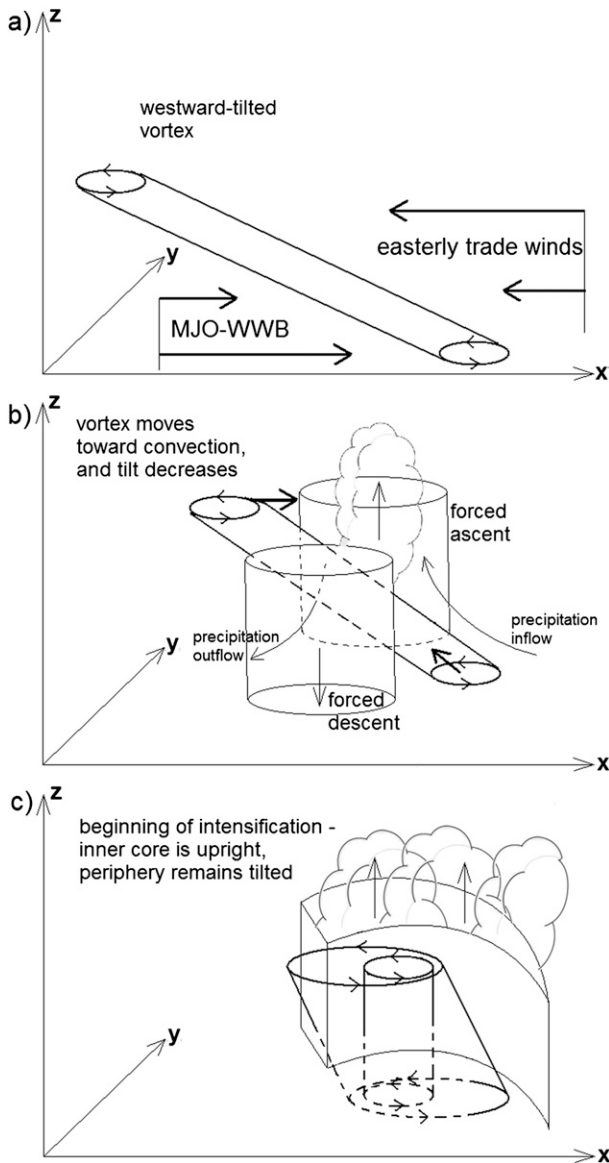
FIG. 14. Conceptual model for (a) the development of a westward-tilted vortex at the interface of the WWB and easterly trades, (b) its associated ascent (descent) on the downtilt-right (downtilt-left) side and the distribution of deep convection on the downtilt-right of the vortex, and (c) the final vertical alignment of the vortex centers leading to the self-sustained intensification.

Third, sustained surface intensification commences as the vortex becomes upright in the vertical (Fig. 14c), despite the fact that the periphery still remains tilted and the northern convection continues as a spiral rainband.

Although previous studies have shown the westward-tilted structures of the MJO/WWB and associated Kelvin and MRG waves in the western Pacific, few have discussed the implications of the tilt on TCG. Of particular importance are the processes associated with the diabatic heating on the downtilt-right side, which precede the transition of the precursor tilted vortex into a vertically coherent TC. A comparison with a dry sensitivity simulation suggests that the diabatic heating indeed plays an important role in determining the northward deviation. Note that this study serves to establish a baseline for the genesis of Chanchu using only the coarse mesh of the quadruply nested simulation. In Part II of this series of papers, we will conduct analyses of mesoscale processes ongoing during the final two days of genesis using the more finely nested simulation dataset, with the goal of clarifying the evolution of the northern convective processes and their impact on impending sustained surface pressure falls.

REFERENCES

Aiyyer, A. R., and J. Molinari, 2003: Evolution of mixed Rossby–gravity waves in idealized MJO environments. *J. Atmos. Sci.,* **60,** 2837–2855.
——, and ——, 2008: MJO and tropical cyclogenesis in the Gulf of Mexico and eastern Pacific: Case study and idealized numerical modeling. *J. Atmos. Sci.,* **65,** 2691–2704.
Barrett, B. S., and L. M. Leslie, 2009: Links between tropical cyclone activity and Madden–Julian oscillation phase in the North Atlantic and northeast Pacific basins. *Mon. Wea. Rev.,* **137,** 727–744.
Bessafi, M., and M. C. Wheeler, 2006: Modulation of south Indian Ocean tropical cyclones by the Madden–Julian oscillation and convectively coupled equatorial waves. *Mon. Wea. Rev.,* **134,** 638–656.
Black, M. L., J. F. Gamache, F. D. Marks, C. E. Samsury, and H. E. Willoughby, 2002: Eastern Pacific Hurricanes Jimena of 1991 and Olivia of 1994: The effect of vertical shear on structure and intensity. *Mon. Wea. Rev.,* **130,** 2291–2312.
Camargo, S. J., M. C. Wheeler, and A. H. Sobel, 2009: Diagnosis of the MJO modulation of tropical cyclogenesis using an empirical index. *J. Atmos. Sci.,* **66,** 3061–3074.
Dickinson, M., and J. Molinari, 2002: Mixed Rossby–gravity waves and western Pacific tropical cyclogenesis. Part I: Synoptic evolution. *J. Atmos. Sci.,* **59,** 2183–2196.
Emanuel, K. A., 1986: An air–sea interaction theory for tropical cyclones. Part I: Steady-state maintenance. *J. Atmos. Sci.,* **43,** 585–605.
Frank, W. M., and E. A. Ritchie, 1999: Effects of environmental flow upon tropical cyclone structure. *Mon. Wea. Rev.,* **127,** 2044–2061.
——, and P. E. Roundy, 2006: The role of tropical waves in tropical cyclogenesis. *Mon. Wea. Rev.,* **134,** 2397–2417.
Gray, W. M., 1998: The formation of tropical cyclones. *Meteor. Atmos. Phys.,* **67,** 37–69.

Hack, J. J., and W. H. Schubert, 1986: Nonlinear response of atmospheric vortices to heating by organized cumulus convection. *J. Atmos. Sci.,* **43,** 1559–1573.

Hogsett, W., and D.-L. Zhang, 2011: Genesis of Typhoon Chanchu (2006) from a westerly wind burst associated with the MJO. Part II: Roles of deep convection in tropical transition. *J. Atmos. Sci.,* in press.

Hong, S.-Y., Y. Noh, and J. Dudhia, 2006: A new vertical diffusion package with an explicit treatment of entrainment processes. *Mon. Wea. Rev.,* **134,** 2318–2341.

Hoxit, L. R., C. F. Chappell, and J. M. Fritsch, 1976: Formation of mesolows or pressure troughs in advance of cumulonimbus clouds. *Mon. Wea. Rev.,* **104,** 1419–1428.

Jiang, X., T. Li, and B. Wang, 2004: Structures and mechanisms of the northward propagating boreal summer intraseasonal oscillation. *J. Climate,* **17,** 1022–1039.

Jones, S. C., 1995: The evolution of vortices in vertical shear. I: Initially barotropic vortices. *Quart. J. Roy. Meteor. Soc.,* **121,** 821–851.

Kain, J. S., and J. M. Fritsch, 1993: Convective parameterization for mesoscale models: The Kain–Fritsch scheme. *The Representation of Cumulus Convection in Numerical Models, Meteor. Monogr.,* No. 46, Amer. Meteor. Soc., 165–170.

Kim, J.-H., C.-H. Ho, H.-S. Kim, C.-H. Sui, and S. K. Park, 2008: Systematic variation of summertime tropical cyclone activity in the western North Pacific in relation to the Madden–Julian oscillation. *J. Climate,* **21,** 1171–1191.

Kuo, H.-C., J.-H. Chen, R. T. Williams, and C.-P. Chang, 2001: Rossby wave in zonally opposing mean flow: Behavior in northwest Pacific summer monsoon. *J. Atmos. Sci.,* **58,** 1035–1050.

Lander, M. A., 1990: Evolution of the cloud pattern during the formation of tropical cyclone twins symmetrical with respect to the equator. *Mon. Wea. Rev.,* **118,** 1194–1202.

Li, X., and B. Wang, 1994: Barotropic dynamics of the beta gyres and beta drift. *J. Atmos. Sci.,* **51,** 746–756.

Liebmann, B., H. H. Hendon, and J. D. Glick, 1994: The relationship between tropical cyclones of the western Pacific and Indian Oceans and the Madden–Julian oscillation. *J. Meteor. Soc. Japan,* **72,** 401–411.

Lin, Y.-L., R. D. Farley, and H. D. Orville, 1983: Bulk parameterization of the snow field in a cloud model. *J. Climate Appl. Meteor.,* **22,** 1065–1092.

Madden, R. A., and P. R. Julian, 1994: Observations of the 40–50-day tropical oscillation—A review. *Mon. Wea. Rev.,* **122,** 814–837.

Maloney, E. D., and D. L. Hartmann, 2000a: Modulation of eastern North Pacific hurricanes by the Madden–Julian oscillation. *J. Climate,* **13,** 1451–1460.

——, and ——, 2000b: Modulation of hurricane activity in the Gulf of Mexico by the Madden–Julian oscillation. *Science,* **287,** 2002–2004.

——, and ——, 2001: The Madden–Julian oscillation, barotropic dynamics, and North Pacific tropical cyclone formation. Part I: Observations. *J. Atmos. Sci.,* **58,** 2545–2558.

Mlawer, E. J., S. J. Taubman, P. D. Brown, M. J. Iacono, and S. A. Clough, 1997: Radiative transfer for inhomogeneous atmospheres: RRTM, a validated correlated-*k* model for the longwave. *J. Geophys. Res.,* **102,** 16 663–16 682.

Mo, K. C., 2000: Intraseasonal modulation of summer precipitation over North America. *Mon. Wea. Rev.,* **128,** 1490–1505.

Molinari, J., and D. Vollaro, 2000: Planetary- and synoptic-scale influences on eastern Pacific tropical cyclogenesis. *Mon. Wea. Rev.,* **128,** 3296–3307.

——, K. Lombardo, and D. Vollaro, 2007: Tropical cyclogenesis within an equatorial Rossby wave packet. *J. Atmos. Sci.,* **64,** 1301–1317.

Nieto Ferreira, R., W. H. Schubert, and J. J. Hack, 1996: Dynamical aspects of twin tropical cyclones associated with the Madden–Julian oscillation. *J. Atmos. Sci.,* **53,** 929–945.

Reasor, P. D., M. T. Montgomery, and L. D. Grasso, 2004: A new look at the problem of tropical cyclones in vertical shear flow: Vortex resiliency. *J. Atmos. Sci.,* **61,** 3–22.

Ritchie, E. A., and G. J. Holland, 1999: Large-scale patterns associated with tropical cyclogenesis in the western Pacific. *Mon. Wea. Rev.,* **127,** 2027–2043.

Roundy, P. E., 2008: Analysis of convectively coupled Kelvin waves in the Indian Ocean MJO. *J. Atmos. Sci.,* **65,** 1342–1359.

Skamarock, W. C., J. B. Klemp, J. Dudhia, D. O. Gill, D. M. Barker, W. Wang, and J. G. Powers, 2005: A description of the Advanced Research WRF, version 2. NCAR Tech. Note NCAR/TN-468+STR, 88 pp.

Sobel, A. H., and E. D. Maloney, 2000: Effect of ENSO and the MJO on western North Pacific tropical cyclones. *Geophys. Res. Lett.,* **27,** 1739–1742.

Sperber, K. R., 2003: Propagation and the vertical structure of the Madden–Julian oscillation. *Mon. Wea. Rev.,* **131,** 3018–3037.

Straub, K. H., and G. N. Kiladis, 2003: The observed structure of convectively coupled Kelvin waves: Comparison with simple models of coupled wave instability. *J. Atmos. Sci.,* **60,** 1655–1668.

Tao, W.-K., J. Simpson, C.-H. Sui, B. Ferrier, S. Lang, J. Scala, M.-D. Chou, and K. Pickering, 1993: Heating, moisture, and water budgets of tropical and midlatitude squall lines: Comparisons and sensitivity to longwave radiation. *J. Atmos. Sci.,* **50,** 673–690.

Webster, P. J., and H.-R. Chang, 1988: Equatorial energy accumulation and emanation regions: Impacts of a zonally varying basic state. *J. Atmos. Sci.,* **45,** 803–829.

Wheeler, M., G. N. Kiladis, and P. J. Webster, 2000: Large-scale dynamical fields associated with convectively coupled equatorial waves. *J. Atmos. Sci.,* **57,** 613–640.

Zhang, C., 2005: Madden–Julian oscillation. *Rev. Geophys.,* **43,** RG2003, doi:10.1029/2004RG000158.

Zhang, D.-L., and K. Gao, 1989: Numerical simulation of an intense squall line during 10–11 June 1985 PRE-STORM. Part II: Rear inflow, surface pressure perturbations, and stratiform precipitation. *Mon. Wea. Rev.,* **117,** 2067–2094.

——, and C. Q. Kieu, 2006: Potential vorticity diagnosis of a simulated hurricane. Part II: Quasi-balanced contributions to forced secondary circulations. *J. Atmos. Sci.,* **63,** 2898–2914.

Zhu, C.-W., T. Nakazawa, and J.-P. Li, 2003: Modulation of twin tropical cyclogenesis by the MJO westerly wind burst during the onset period of 1997/98 ENSO. *Adv. Atmos. Sci.,* **20,** 882–898.